Chapter 3   **Direct evidence of an efficient Plasmon-induced hot-electron transfer at** *in situ* **grown Ag/TiO$_2$ interface for highly enhanced solar H$_2$ generation**

3.1 Introduction

Plasmon induced hot-electron generation and its efficient transfer from metal nanoparticles to the semiconductor is an effective route for solar energy conversion in photovoltaic and photocatalytic devices [77-81]. Due to the Surface Plasmon Resonance (SPR) phenomenon, metal nanoparticles (NPs) are capable of absorbing light by exciting Localized Surface Plasmon (LSP)[78, 82]. After light absorption, these LSP can decay either radiatively through re-emit of photons or non-radiatively via hot electron-hole pair formation within the metal NPs via Landau damping process in a time scale of 1-10 fs [78, 82, 83]. These hot electrons are not in thermal equilibrium and occupy the energy level above the Fermi energy. To utilize these hot-electrons for solar energy conversation, it is required an efficient charge transfer to the conduction band (CB) of a semiconductor charge transport layer within a time scale of 100 fs to 1 ps[78]. Otherwise, hot-electron will lose their extra energy by the electron-electron scattering process via thermal conduction within hundreds of femtoseconds [82]. Schottky junction formation at the interface of metal NP is an established route to capture this hot electron to the conduction band (CB) of semiconductors[78, 82]. After the injection of hot-electrons into the CB of the semiconductor, the metal NPs becomes positively charged. An electron-donating electrolyte solution or a hole-transport material (HTM) is needed to be in contact with the metal NPs to transport the plasmon generated holes to the counter electrode [78]. Therefore, authors are finding an efficient electron-hole separation schemes for efficient conversion of solar energy.

Till now, a large number of reports have been published for the enhancement of charge transfer rate of hot-electron generated by LSP [67, 81, 84]. In addition, several strategies have been taken to utilized plasmon-induced hot-carrier in photovoltaic and photocatalytic devices [67, 81, 84-86]. However, the efficiency of most of these devices is very poor for practical application, and 'incident photon to current efficiency' (IPCE) is too low for the realization of the impact of hot-electron on photocurrent generation [77, 79, 80, 87, 88]. The key reason for this low efficiency comes due to the low charge transfer rate from plasmonic metal NP to the CB of semiconductor that depends on the nanostructure of metal NP, the location of metal NP relative to neighbouring semiconductor and metal NP/semiconductor interface trap state [78, 82]. In most previous studies, metal NPs is deposited on top of an oxide semiconductor by different deposition method that forms a poor metal/semiconductor interface with the lower interfacial area and with higher interface trap state, resulting in a significantly lower charge transfer rate [80, 88, 89]. Again, it has been reported earlier that hot-electron generation and its transport can be highly enhanced by embedding metal nanostructure inside a semiconducting material [90]. Therefore, a unique fabrication scheme required to fulfill the criteria of the higher charge transfer rate of hot-electron.

In this study, a unique solution-processed approach has been taken to develop *in situ* grown Ag NPs within titanium oxide (TiO_2) thin film. This low cost and large area deposition technique allow us to fabricate Ag-NP surrounded by TiO_2 semiconductor and has been utilized for photocatalytic H_2 generation. This thin film growth consists of three successive steps, including sol-gel derived ion-conducting thin film fabrication containing loosely bound light ion (Li^+) followed by ion-exchanged (with Ag^+) and subsequent

reduction process. The Ag-TiO$_2$ thin film that grown by this technique is contained Ag NPs with size ranging from 10 to 20 nm. The size and inter-particle distance of Ag-NPs can be controlled by changing the growth conditions. The highly efficient photo-electro-catalytic performance of Ag-TiO$_2$ composite thin films was identified by a photo-electrochemical water splitting experiment, which shows a significantly higher performance than earlier reported Ag-TiO$_2$ composite thin-film, has been discussed in subsequent sections. An intense photocurrent generation has been identified in the region of plasmonic absorption of Ag NPs by measuring 'incident photon to current efficiency'(IPCE) data in the different frequency range of incident light, reveals the strong contribution of plasmon-induced hot-electron for the enhancement of photocatalytic H$_2$ generation. A transfer-enhancement synergistic mechanism has been proposed to explain these experimental results.

3.2 Results and Discussions

3.2.1 Structural and Surface morphology characterization

The crystal structure and phase confirmation of those thin films were analyzed by using a Rigaku X-ray diffractometer with Cu-Kα radiation (λ = 1.54 Å) in the 2θ range of 15º–70º with a scan rate of 2θ were 2°/min. The X-ray diffraction (XRD) patterns of the samples were collected at room temperature. **Figure 3.1(a)** (red) shows the x-ray diffraction (XRD) pattern of pure Li4Ti5O12 (LTO) dip-coated thin film that has been deposited on the Si substrate. The diffraction peaks of LTO of located at 2θ ~ 18.5, 35.6, 43.7, which correspond to the reflection planes of (111), (311), (331) that have been well matching with JCPDS file no. 490207, indicates the cubic spinel structure with the space group of ($F\bar{3}dm$). The diffraction peaks of Ag-TiO$_2$ thin film that has been shown in

figure 3.1(a) (black) indicates the peak positions at 2θ ~38.12^0, 44.307 for Ag NPs that

appears from the diffraction planes of (111), (200), respectively (JCPDF no. 893722).The TiO$_2$ has three different crystallographic phases of (i) rutile (ii) anatase and (iii) brookite and among these phases, anatase is thermodynamically more stable than rutile and brookite. This XRD study of Ag-TiO$_2$ thin film has identified the formation of the anatase phase that has a peak position at 2θ ~25.35^0.

Figure 3.1(b) shows the UV-VIS absorption spectra of different photoanodes covering the range of 320-900 nm. Absorption spectra of TiO$_2$ thin film show strong absorption in the UV region (300-350 nm) with a steadily lower absorption in higher wavelength light, which is expected from wide bandgap TiO$_2$ thin film. On the other hand, in the case of Ag-TiO$_2$ thin film, it shows a strong plasmonic absorption peak of Ag at 433 nm due to the formation of Ag nanocrystal inside the thin film. This plasmonic absorption peak should be attributed to the SPR effect due to the Ag NPs formation inside the TiO$_2$ matrix (**Figure 3.1 (b)).** The variation of particle size of Ag-NP can changes the peak position of plasmonic absorption. Besides, percentage of absorption also varies with particle size. Long tail of this Ag-TiO$_2$ thin film absorption spectra is due to the distribution of particle size of Ag-NP. This plasmonic absorption due to the SPR effect becomes stronger in the case of Ag-TiO$_2$/TiO$_2$ sol-gel and Ag-TiO$_2$/TiO$_2$ NP coated photoanodes w.r.t Ag-TiO$_2$ because of the hot electron transfer to the additional TiO2 layer of Ag-TiO$_2$/TiO$_2$ sol-gel, and Ag-TiO$_2$/TiO$_2$ NPs coated films. In a similar process, we have grown Cu NP inside the TiO$_2$ matrix. UV-absorption of Cu NPs-TiO$_2$ thin film is shown in (Figure 3.1(d)) which indicates a clear plasmonic absorption peak at 594 nm which is similar to earlier report [91].

3.2.2 The surface morphology and microstructure characterization

40

The detail of surface morphology and Ag nanoparticle size were investigated by high resolution-scanning electron microscopy (HR-SEM), which shown in figure 3.2.Samples were prepared on highly doped Si or Glass substrate by dip-coating method. Dip coating samples were prepared with a dipping speed of 2 mm/s, followed by an annealing process.
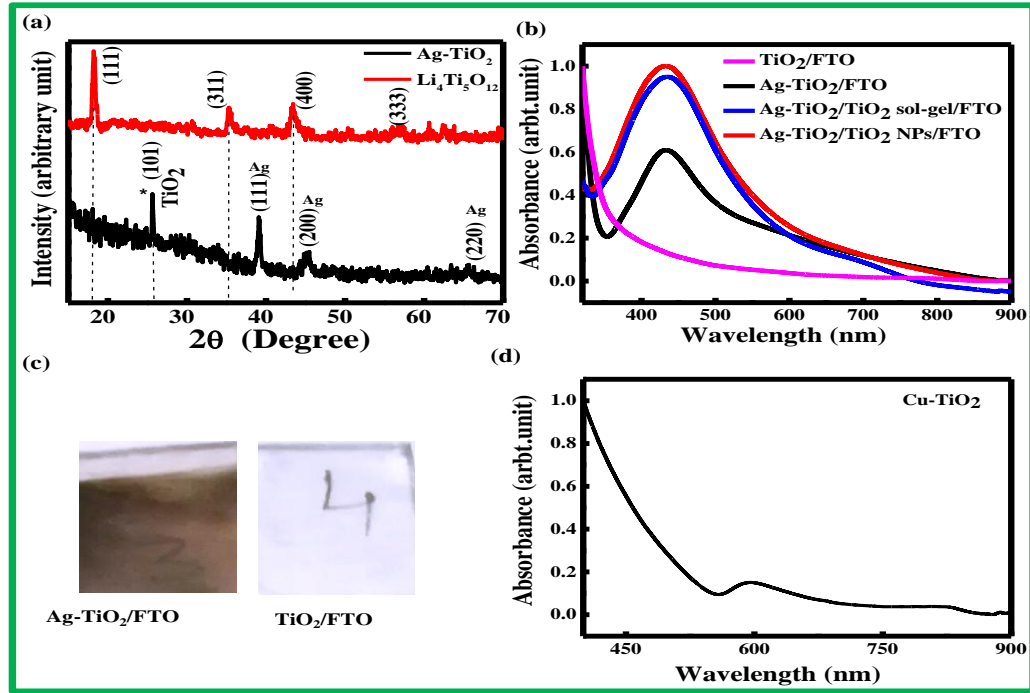

Figure 3.1: (a) The XRD pattern of LTO and Ag-TiO₂, (b) normalized UV-VIS absorption spectra of different photoanodes coated with TiO₂, Ag-TiO₂, Ag-TiO₂/TiO₂ sol-gel, and Ag-TiO₂/TiO₂ NPs, respectively.(c) The sample images of Ag-TiO₂ and TiO₂ thin films,(d) UV-VIS absorption spectra of Cu-TiO₂ thin film.

After that, all these samples undergo through ion-exchange and reduction process to grow Ag-TiO₂ thin film. **Figure 3.2(a)** shows the Ag-TiO₂ film prepared by a dip-coating method with a concentration of 300 mM which indicates the Ag nanocrystal formation inside the TiO₂ matrix. Additionally, it gives information about the size of Ag NPs, which **are** spherical in shape with an average particle size of 13 nm. The distribution of particle size has been shown in **figure 3.2 (b),** which indicated the particle size is mostly varied within the range from 10 nm to 20 nm. The composition and content of the metallic
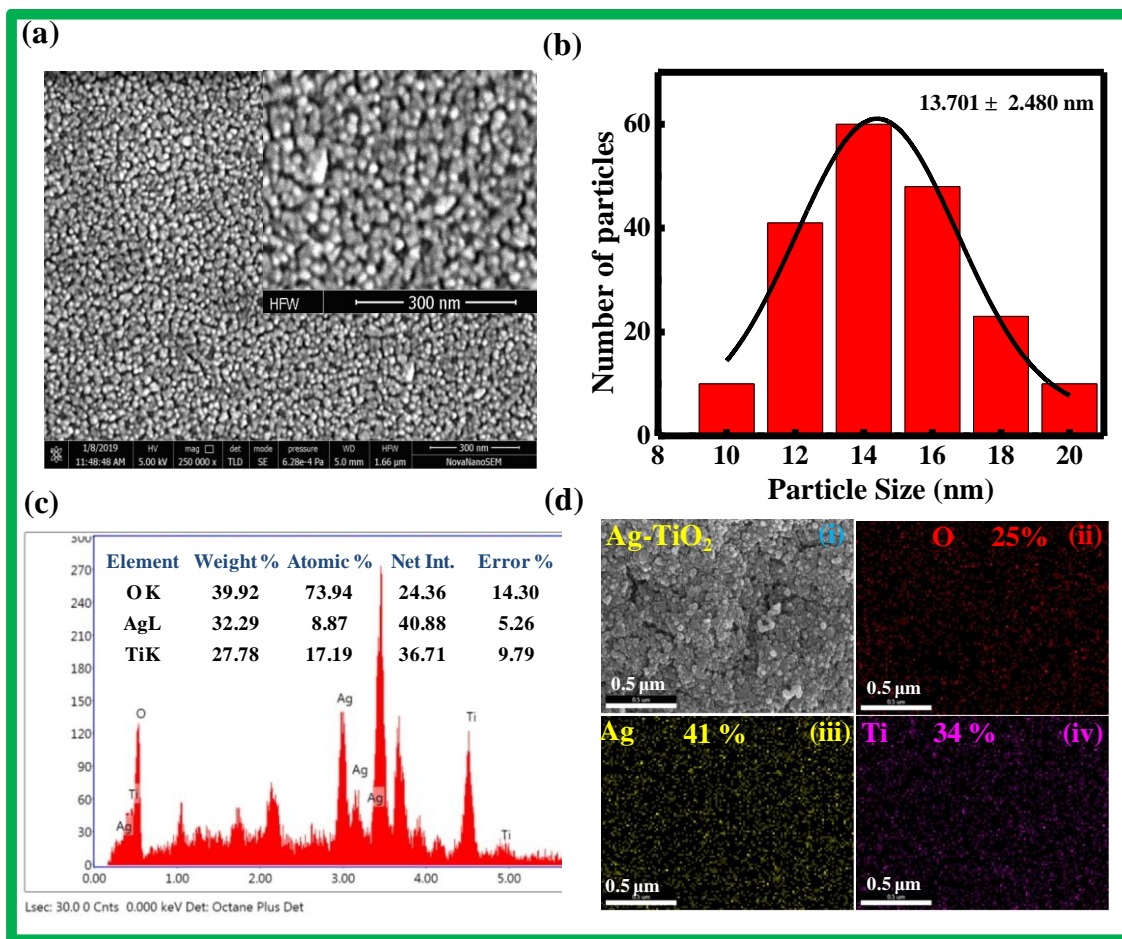
(a)

HFW | 300 nm

1/8/2019 11:48:48 AM | HV 5.00 kV | mag □ 250 000 x | det TLD | mode SE | pressure 6.28e-4 Pa | WD 5.0 mm | HFW 1.66 µm | 300 nm | NovaNanoSEM

(b)

13.701 ± 2.480 nm

Number of particles

Particle Size (nm)

(c)

Element	Weight %	Atomic %	Net Int.	Error %
O K	39.92	73.94	24.36	14.30
AgL	32.29	8.87	40.88	5.26
TiK	27.78	17.19	36.71	9.79

Lsec: 30.0 0 Cnts 0.000 keV Det: Octane Plus Det

(d)

Ag-TiO₂ (i)   O   25%   (ii)
0.5 µm   0.5 µm

Ag   41 %   (iii)   Ti   34 %   (iv)
0.5 µm   0.5 µm

Figure 3.2: The surface morphology of the (a) **Ag-TiO2 (dip coated) thin film** *on Si substrate (b) Particle size distribution of Ag-NPs inside TiO$_2$ thin film, (c) Energy dispersive spectra of Ag-TiO$_2$ thin film, an elemental composition that obtained from EDS shown in the inset. (d) EDS mapping of Ag-TiO$_2$ thin film (i) original SEM image on the FTO substrate (ii) for O, (iii) for Ag, and(iv) for Ti.*

element of the Ag-TiO$_2$ samples were determined by an energy-dispersive X-ray spectrometer (EDX) attached to the HR-SEM **(Figure 3.2(c))**.This picture clearly shows the existence of Ag and Ti elements inside thin film. **Figure 3.2(d)** shows the EDS mapping for Ag-TiO$_2$ thin film to ensure the existence of Ag, Ti and O, and distribution in a different part of the thin film. Their uniform distribution confirms the uniform growth of Ag NPs throughout the film. Transmission electron microscopy (TEM) study has been

42

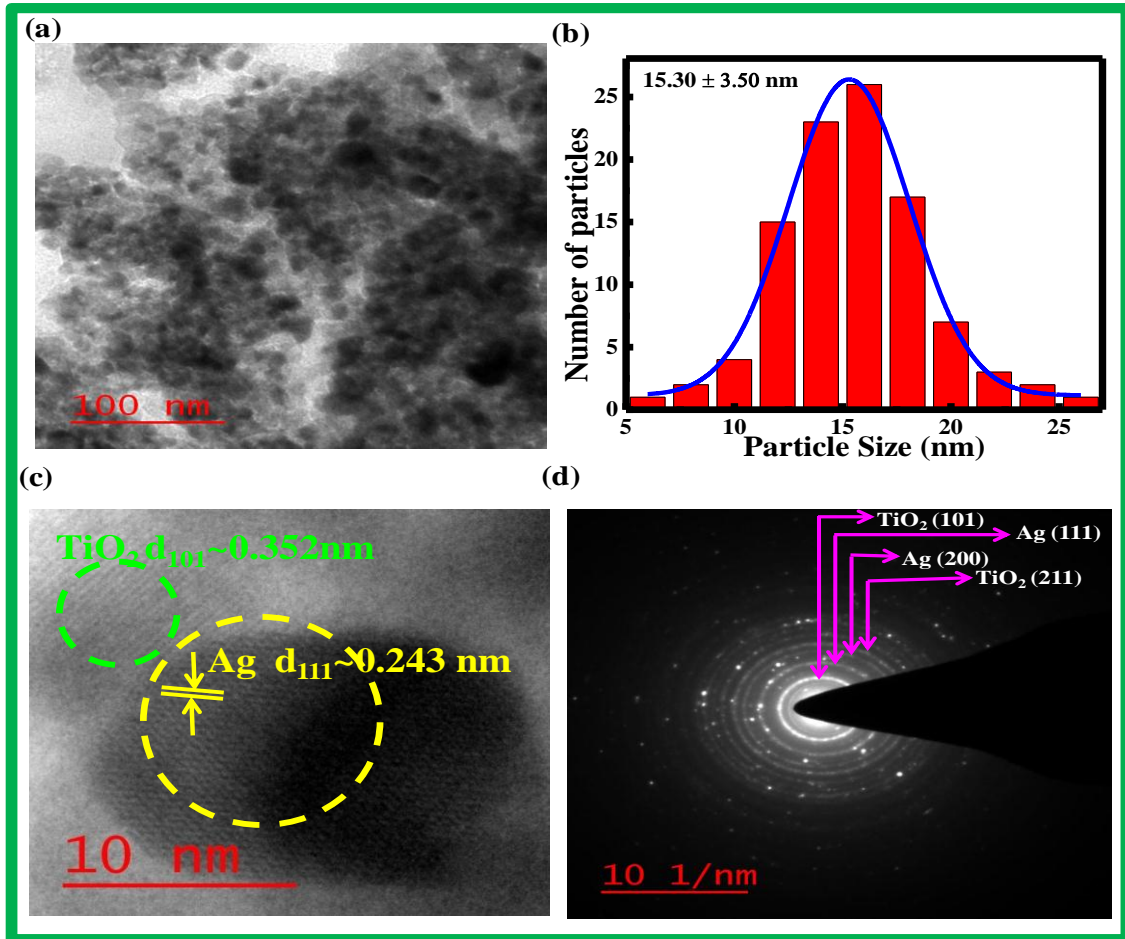done to determine the Ag particle size and distribution and its coexistence with the TiO_2 matrix.

Figure 3.3 *(a) Transmission electron microscope image of Ag NPs-TiO_2thin film,(b) particle size distribution of Ag NPs inside TiO_2 thin film, (c) high-resolution image of Ag NPs-TiO_2, the green circle indicates the lattice spacing d-fringe of Ag and yellow circle for TiO_2 (d) selected area electron diffraction (SAED) pattern of Ag NPs-TiO_2.*

For the TEM study, thin film material of Ag-TiO_2 was scratched from the substrate and made a fine powder of the Ag-TiO_2 sample by using a grinding mortar. Then this powder sample was dispersed in chloroform by keeping the solution under an ultrasonic bath for 1 hour. **Figure 3.3(a)** shows the TEM image with relatively lower magnification that indicated a dense Ag-NPs is grown in the TiO_2 matrix. This picture also shows that the

particle size is distributed mostly within the range of 10-20 nm. Particle size distribution has been shown in **figure 3.3(b)** that indicates the average particle size of Ag-NP is 15 nm.
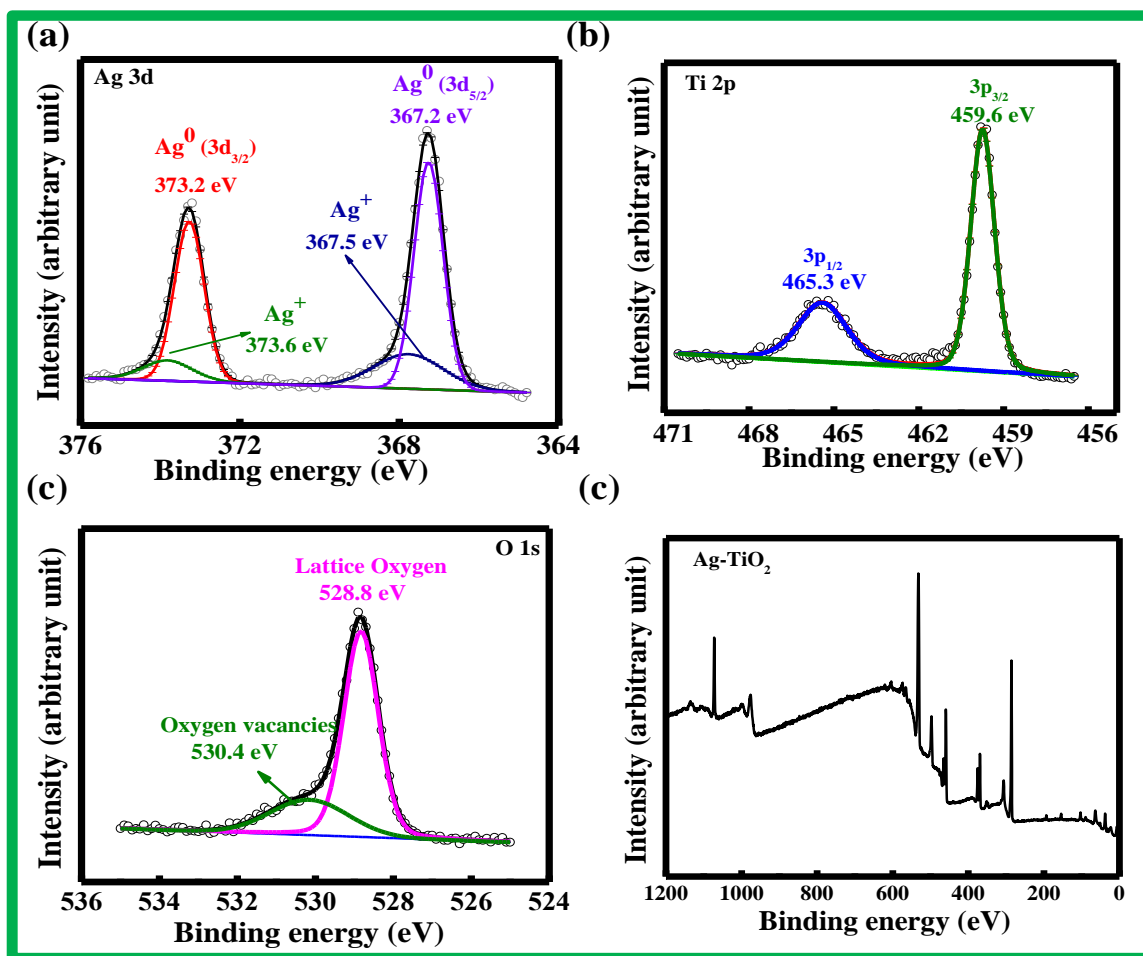

Figure 3.4: *High-resolution XPS spectra of Ag-TiO$_2$ sample (a) Ag 3d (b) Ti 2p and (c) O 1s. (d) The full scan of XPS for the Ag-TiO$_2$ thin film.*

This distribution is very much similar to SEM analysis. High-resolution image (**figure 3.3(c)**) of Ag-TiO$_2$ shows the lattice fringe formation of Ag-NP and TiO$_2$ individually and Their co-existence. The averaged d-spacing value of Ag-NP is 0.24 and 0.34 nm, respectively that are corresponding to Ag (111) and anatase TiO$_2$ (101) plans. In XRD analysis of the Ag-TiO$_2$ sample (**Figure 3.1(a)**, these two respective planes of Ag and TiO$_2$ also show the most intense peak. As reported earlier, such interconnection between Ag-NPs

44

and TiO_2 always favors photo generated electron transfer by reducing carrier recombination [92]. **Figure 3.3(d)** shows the selected area electron diffraction (SAED) pattern of Ag NP-TiO_2 sample that clearly shows multiple diffraction ring formation by Ag NPs and TiO_2. The diffraction ring has been identified from (111), (200) and (220) planes of Ag. Similarly, TiO_2 gives the diffraction ring from (101) and (211) planes. Summary of different diameters of diffraction ring and corresponding planes are shown in **table-3.1**.

Table 3.1- The summary of diameter for diffraction ring and corresponding planes from SAED.

Name of the element	Diameter (nm)	Radius (nm)	Spacing (d)	(hkl)
TiO_2	5.649	2.824	0.34	101
Ag	8.257	4.1285	0.24	111
TiO_2	10.550	5.275	0.18	200
TiO_2	11.965	5.982	0.16	211
Ag	13.448	6.724	0.14	220
TiO_2	14.891	7.4245	0.13	116

3.2.3   X-ray photoemission spectroscopy (XPS)

X-ray photoemission spectroscopy (XPS) study was conducted to investigate the chemical oxidation state of the elements present in Ag-TiO_2 thin film (**shown in figure 3.4**). The sample for this study was prepared on a glass substrate by a single time dip coating with an LTO precursor. The XPS spectra of Ag 3d, Ti 2p, and O 1s are shown in **figure 3.4(a), 3.4(b), and 3.4(c),** respectively. **Figure 3.4(a)** shows that the Ag 3d has two intense peaks at 373.2 and 367.2 eV which corresponds to the binding energy of Ag $3d_{3/2}$ and Ag $d_{5/2,}$ respectively. Similarly, two peaks appear with intensities of Ti $2p_{1/2}$ and Ti $2p_{3/2}$ at 465.3 eV and 459.6 eV which are characteristic for Ti^{+4}, are shown in figure 3.4(b).

Two peaks (**Figure. 3.4(c)**) appear for O 1s at the binding energies of 528.8 eV, 530.4 eV which correspond to O in TiO_2 and oxygen vacancies respectively. All these peak positions are well –matched with earlier reported of Ag-TiO_2 systems [68, 93].Therefore, the XPS study of this sample gives another proof of the formation of Ag-TiO_2 film.

3.2.4   Photoelectrochemical H_2 generation study

Figure 3.5(a) shows the photoelectrochemical properties for different Ag-TiO_2 thin films in 1 M KOH solution under white light (1000 W/m^2) and dark conditions. As shown, for all three different types of Ag-TiO_2photoanodes, there is around one order difference of current between light and dark conditions. Again photocurrent of Ag-TiO_2 photoanodes increases considerably in addition to underlying TiO_2 thin film. The highest photocurrent was observed with Ag-TiO_2/TiO_2 NPs/FTO photoanode with a current density of 42 mA cm^{-2} at -0.45 V external bias. To the best of our knowledge, this current density is significantly higher with respect to earlier publications on Ag/TiO_2 system. In **table-3.2**, a summary of earlier key publications on the Ag/TiO_2 system has been compared with our current observation. From this comparison, it's very clear that this Ag-TiO_2 thin film is superior with respect to the earlier reported Ag-TiO_2 photocatalysis. Again, this current density is 4200 times higher comparing to TiO_2 (only) coated photoanode (0.01 mA cm^{-2}) under the same visible light illumination **figure 3.6(a)**. This enhancement is due to efficient plasmon-induced hot-electron generation inside metal NPs and its non-radiative decay to electron-hole pair during visible light illumination. This energetic electron then transferred to the conduction band TiO_2 through the energy transfer process and transported to the FTO electrode. Finally, this photogenerated electron reaches to counter platinum (Pt) electrode and generate H_2 gas at cathode [94, 95].This phenomenon occurs in parallel to the

conventional photocurrent generation by TiO₂ under the illumination of UV light. The mechanism of H₂ generation has been schematically presented in **figure 3.5(b)**.Due to the irradiation of high energy photon (UV),the valance band electrons of TiO₂ excited to the conduction band (equation (3.1). After reaching the conduction band of TiO₂, electrons are migrated to the FTO electrode.
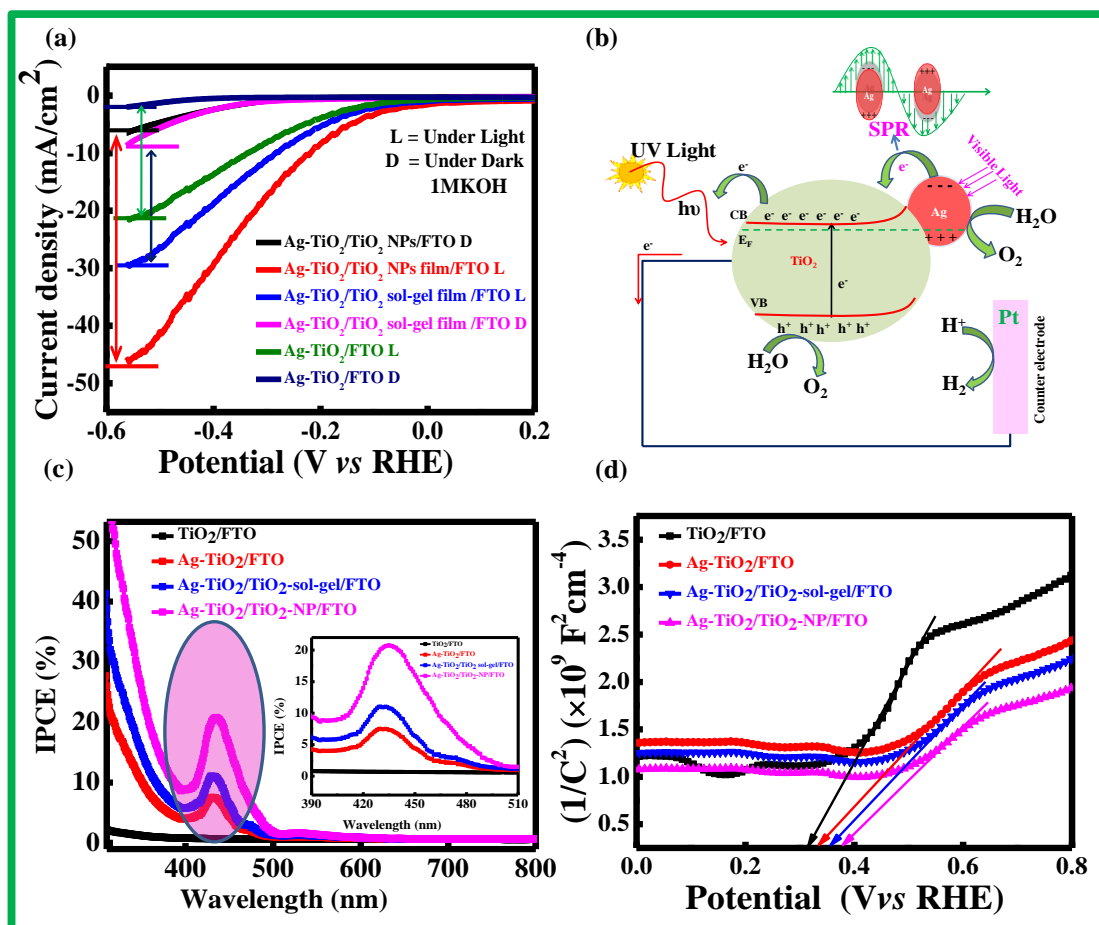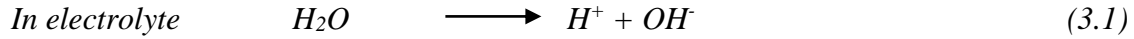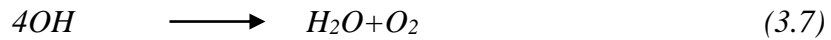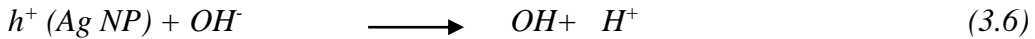

Figure 3.5 *(a) Current density vs. (V vs.RHE) potential of different Ag-TiO₂ thin film under light and dark in 1 M KOH solution (b) schematic diagram of photocatalytic water splitting mechanism by Ag-TiO₂ based photoanode due to the SPR effect of Ag NPs. (c) IPCE data for different photoanode in the range of 350 nm to 800 nm under -1.0V external bias with 1 M KOH electrolyte solution. Inset shows the magnified IPCE data in the wavelength range from 390 nm to 510 nm. (d) Mott−Schottky (M-S) plot for different photoanodes in 1 kHz operation under dark condition.*

In addition, the photogenerated hole of the valance band of TiO$_2$ is captured by OH$^-$ of electrolyte to generate O$_2$ gas at the anode which is a conventional photoelectrochemical effect by TiO$_2$ equations (3.2) and (3.3). However, the major contribution of the photogenerated electron is coming due to the surface Plasmon resonance (SPR) effect of Ag NPs, which gives a large enhancement of photocurrent density (**figure 3.5 (a)**). Due to this SPR process, energetic electrons are generated inside Ag NP that immediately transfers to the conduction band of TiO$_2$ through the energy transfer process and transport to the FTO electrode (figure 3.5(b), equation (3.4). Finally, this SPR induced photogenerated hot-electron reaches to the counter electrode, where it reduces H$^+$ to H to form H$_2$ gas (equation (3.8)). In addition, the positive charge of Ag NPs, oxidize OH$^-$ to form O$_2$ at anode equation (3.5) to equation (3.7) [94, 95].

In electrolyte $\qquad$ H_2O $\qquad \longrightarrow \qquad$ $H^+ + OH^-$ $\qquad\qquad$ *(3.1)*

At Anode

$\qquad$ $TiO_2 + hv \ (UV \ light)$ $\qquad \longrightarrow \qquad$ $h^+ \ (VB_{TiO_2}) + e^- \ (CB_{TiO_2})$ $\qquad$ *(3.2)*

$\qquad$ $h^+ \ (VB) + OH^-$ $\qquad \longrightarrow \qquad$ $OH + \ H^+$ $\qquad\qquad$ *(3.3)*

$\qquad$ $(Ag \ NPs) + hv \ (visible)$ $\qquad \longrightarrow \qquad$ $e^- \ (SPR)$ $\qquad\qquad$ *(3.4)*

$\qquad$ $e^- \ (Ag \ NP, \ SPR \ induced)$ $\qquad \longrightarrow \qquad$ $To \ CB_{TiO_2}$ $\qquad\qquad$ *(3.5)*

$\qquad$ $h^+ \ (Ag \ NP) + OH^-$ $\qquad \longrightarrow \qquad$ $OH + \ H^+$ $\qquad\qquad$ *(3.6)*

$\qquad\qquad$ $4OH$ $\qquad \longrightarrow \qquad$ $H_2O + O_2$ $\qquad\qquad$ *(3.7)*
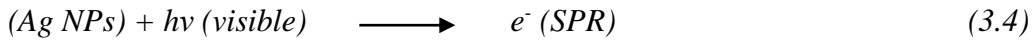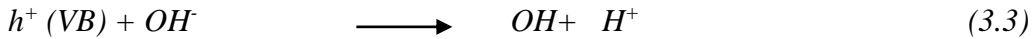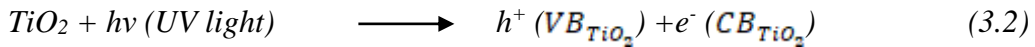
At Pt counter electrode (Cathode)

$\qquad\qquad$ $2H^+ + 2e$ $\qquad \longrightarrow \qquad$ H_2 $\qquad\qquad$ *(3.8)*

3.2.5 IPCE measurement

For a better understanding of the enhancement of the photocurrent under visible light illumination, IPCE measurement has been done in different wavelengths of light. **Figure 3.5(c)** shows the comparative IPCE data of different Ag-TiO$_2$ photoanode under -1.0 V

external bias. The TiO_2 (sol-gel) coated photoanode has been used as a reference for this measurement. As it is seen from **figure 3.5(c),** the IPCE spectrum of all Ag-TiO_2 photoanode is very much similar in nature with a very strong photocurrent generation in the region of plasmonic absorption of Ag-TiO_2 thin film **(figure 3.1(b))** with a peak position at 435 nm. Since TiO_2 has is a wide bandgap semiconductor with a bandgap of 3.3 eV; therefore, the contribution of photocurrent from TiO_2 always exists bellow 400 nm. This nature of IPCE spectra clearly indicated that the major part of photocurrent associated with H_2 generation is originated from the plasmon-induced hot-electron (shaded area of **figure 3.5(c)**

Table 3.2: The photocurrent density of the various type of Ag coated TiO_2 based photoanodes.

Device structure	Electrolyte and illumination condition	Current density	Stability	Reference
$Bi_2S/Ag_2S/TiO_2$	Neutral pH phosphate buffer solution	0.08 mA/cm^2	300 s	*Chem. Comm.*, 2018, **54**, 806-809[96]
Ag/TiO_2	Aqueous methyl blue solution	15 nA/cm^2	-	*Chem. Mater.*, 2008, **20**, 6543-6549[97]
Ag/TiO_2 Nanotube arrays	0.2 M H_3PO_4 and 0.3 M NH_4F solution	40 µA/cm^2	-	*J. Alloy Compd*, 2013, **554**, 72-79[98]
Ag/N-TiO_2 Nanotube arrays	1 M KOH solution	2.5 µA/cm^2	-	*J. Am. Chem. Soc.*, 2011, **133**, 5202-5205[66]
Ag/n-TiO_2 Nanotubes	Methyl Orange solution	0.12 mA/cm^2	-	*Electrochimica Acta*, 2010, **55**, 7211-7218[99]
Ag/n-TiO_2Nanorod	0.5M Na_2SO_4	1.52 mA/cm^2	10	*Ind. Eng. Chem. Res.*, 2019, **58**, 4818-4827[68]
Ag-TiO_2+SCN	0.2 M, [MeOH]	16 mA/cm^2	-	ACS Catal. 2016, 6, 821−828[67]
Ag/n-TiO_2 Nanoparticles	1 M KOH solution	**42.0 mA**/cm^2	**>1.5hrs**	**Present work**

Again, comparative IPCE studies of different Ag-TiO$_2$ photoanode shows that the highest value of IPCE has been achieved for the Ag-TiO$_2$/TiO$_2$ NPs/FTO sample with a value of ~ 22% at 435 nm. This data implies that addition TiO$_2$ under layer help smuch faster charge transfer to the FTO electrode. Comparing TiO$_2$ NPs and TiO$_2$ sol-gel thin film, the earlier one is better choice to use as an additional charge transfer layer. Most likely, it's due to the better crystallites of TiO$_2$ NPs thin film. The magnified picture of IPCE data (inset, **figure 3.5 c**) shows that the photocurrent TiO$_2$ photoanode is negligibly small and doesn't have any significant value around 435 nm.

3.2.6 AC impedance study and Mott−Schottky (M-S) measurements

Further, the Mott−Schottky (M-S) measurements were carried out for a more detail understanding of the hot-electron transport properties. This measurement has been carried out on different photoanodes coated with pure TiO$_2$, Ag-TiO$_2$, Ag-TiO$_2$/TiO$_2$ sol-gel, and Ag-TiO$_2$/TiO$_2$ NPs at an applied frequency of 1 kHz under dark conditions. The flat band potential (E$_{FD}$) of the semiconductor-electrolyte interface and the surface charge density (N$_D$) values were estimated using the Mott−Schottky equation (3.9).

$$\frac{1}{C^2} = \frac{2}{e\,\varepsilon_0\,\varepsilon_r N_D}\left(E_{app} - E_{FD} - \frac{kT}{e}\right) \qquad (3.9)$$

Where, C is the interfacial capacitance, E$_{FD}$ is the flat band potential, k (1.3807×10^{-23}) is the Boltzmann constant; e is the electronic charge (1.6×10^{-19} coulomb), and T is the temperature of the system (~300K). The Mott−Schottky plot for different photoanodes which is the linear variation of $1/C^2$ with respect to the applied potential is shown in **figure 3.5(d).** Positive slopes of individual plots indicated the n-type semiconductor nature of all photoanodes. The flat band potential (E$_{FD}$) of the photoanode can be determined from the

intercept of the slope with the x-axis of the plot. A positive shift of E_{FD} has been observed in all Ag-TiO$_2$ photoanodes with respect to the TiO$_2$ (only) photoanode, indicates a significant improvement of charge transfer rate due to the Ag-TiO$_2$ thin film formation. This M-S plot doesn't vary much within the AC frequency range 100 Hz to 1000kHz, indicates the existence of very low surface state. The highest value of E_{FD} has been observed for Ag-TiO$_2$/TiO$_2$ NPs coated photoanode, which implies the most efficient charge transfer rate among four different photoanodes. The surface charge density (N_D) has been calculated by using the slop of the M-S plot which is related by the following equation (3.10).

$$N_D = \frac{2}{e\varepsilon_0\ \varepsilon_r} \frac{dE}{d(\frac{1}{C^2})}$$

(3.10)

This calculation indicates the values of N_D are largely enhanced due to the Ag-TiO$_2$ thin film formation with respect to TiO$_2$ (only) thin film. The highest value of N_D has been observed for Ag-TiO$_2$/TiO$_2$ NPs thin film, which is responsible for the reduction in the ohmic resistance of the film that leads to improving the higher rate charge transfer from photoanode to the FTO electrode. The summary of E_{FD} and N_D values for all of these photoanodes are summarized in **table-3.3**.

Table 3.3: The flat band potential and surface charge density (N_D) at 1 kHz for the different devices is summarized.

Name of the Device	Flat band potential (V)	N_D (cm^{-3})
TiO$_2$/FTO	0.30	8.87×10^{17}
Ag-TiO$_2$/FTO	0.33	3.39×10^{18}
Ag-TiO$_2$/TiO$_2$ sol-gel /FTO	0.35	3.69×10^{18}
Ag-TiO$_2$/TiO$_2$ NPs/FTO	0.37	4.85×10^{18}

Figure 3.6 (c) shows the electrochemical impedance spectroscopy (EIS) measurement for three different Ag-TiO$_2$ photoanodes under light and dark conditions. As observed, there is a big difference in EIS data under dark and light for all these photoanodes, indicating a large variety of resistances under these two conditions. The comparative EIS study shows that the semicircles of Ag-TiO$_2$/TiO$_2$ NPs/FTO have smaller semicircles than two other photoanodes both under dark and light conditions, which implies the resistance of this sample is least than two others. Moreover, the smaller semicircle suggests faster charge transfer and separation rate of photo generated electron-hole than other samples. Inset shows the equivalent circuit of photoelectrochemical measurement set-up that includes the solution resistance (R$_S$) in series with the parallel connection of interfacial charge-transfer resistance of the photoanode/electrolyte interface (R$_1$) and double-layer capacitance (C$_1$) associated with the charge transfer process. All EIS data are fitted according to this equivalent circuit. The value of R$_1$ is summarized of all three Ag-TiO$_2$ photoanodes under light and dark conditions and shown in the **table-3.4**.

Table 3.4: Fitting value of R$_1$data for all different samples under dark and light conditions.

Samples	Under Dark R$_1$ (kΩ)	Under Light R$_1$ (kΩ)
Ag-TiO$_2$/FTO	4.041	0.707
Ag-TiO$_2$/TiO$_2$ sol-gel /FTO	3.210	0.611
Ag-TiO$_2$/TiO$_2$ NPs/FTO	3.001	0.521

Table 3.5: The rise and fall time from time response data of different photoanodes are summarized.

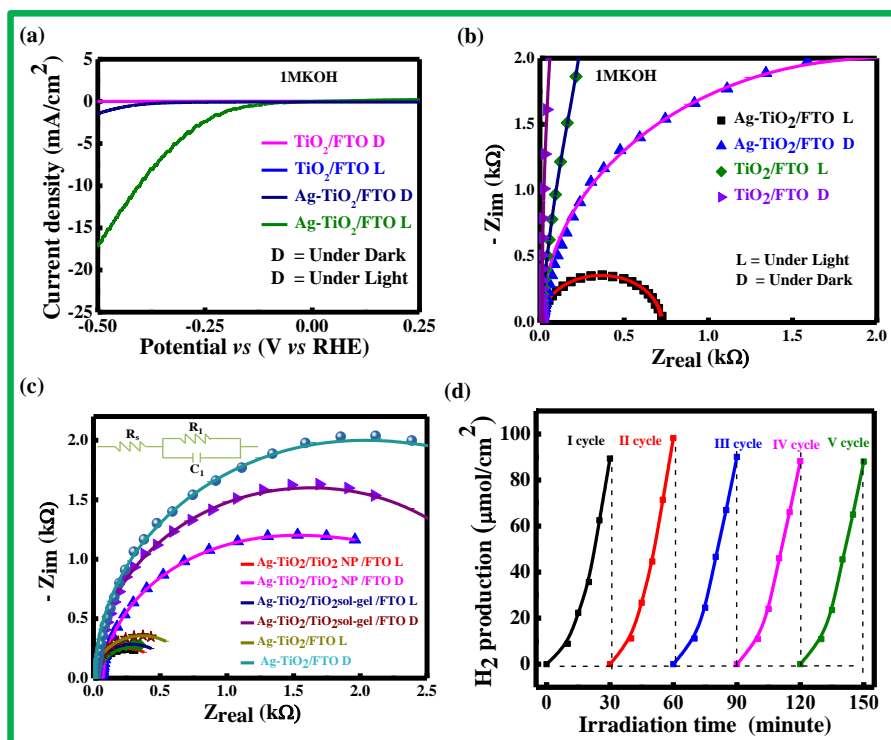| Name of the Sample	Raising time	Falling time
TiO$_2$/FTO	1.21 Sec.	2.40 Sec.
Ag-TiO$_2$/FTO	0.68 Sec.	1.63 Sec.
Ag-TiO$_2$/TiO$_2$ sol-gel /FTO	0.87 Sec.	1.60 Sec.
Ag-TiO$_2$/TiO$_2$ NPs/FTO	0.60	1.60

Figure 3.6: (a) Current density vs. (V vs. RHE) potential of Ag- TiO_2 and TiO_2 thin film (b) The EIS spectra for Ag- TiO_2 and TiO_2 photoanodes. (c) The EIS spectra of three different Ag- TiO_2 photoanodes under light and dark in 1 M KOH solution. The inset shows the equivalent circuit. (d) Volumetric hydrogen generation over the time in five different cycles for Ag- TiO_2/ TiO_2 NPs/FTO photoanode under one sun white light irradiation.

Comparative EIS studies between Ag- TiO_2/FTO and TiO_2 sol-gel/FTO photoanodes are shown in **figure-3.6(b)** that shows the formation of Ag NPs inside TiO_2 thin film reduce the resistance of the photoanode both under dark and light conditions.

3.2.7 Volumetric hydrogen generation rate and time response measurement

The volumetric hydrogen generation over time has been analyzed by continuous irradiation by the white light of one sun and by collecting generated hydrogen. This experiment has been performed for Ag- TiO_2/ TiO_2 NPs/FTO photoanode. As it is shown in **figure-3.6(d)**, this rate is initially slower, and over time, it becomes almost constant. Under 30-minute irradiation, the amount of H_2 that has been collected is ~90 µmol/cm². This experiment has been repeated for five successive cycles that show almost similar results.
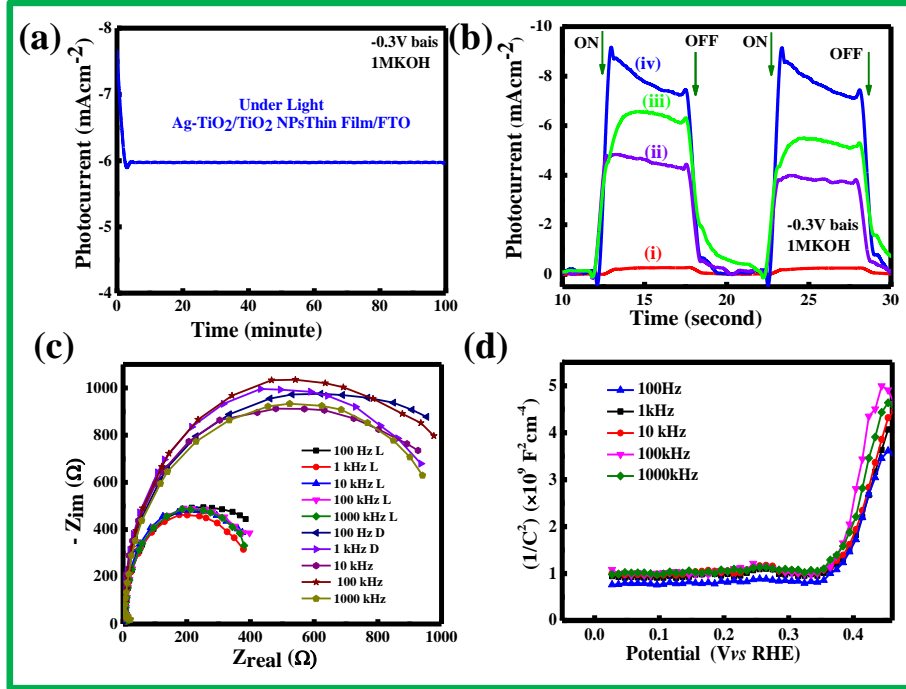
Figure 3.7*(a) Photostability tested for Ag-TiO$_2$/TiO$_2$ NPs/FTO thin film under continues light illumination in 1M KOH solution. (b) Time response of different photoanode under light (100 mw/cm^2) with -0.3 V external bias, (i) for TiO$_2$/FTO (ii) for Ag-TiO$_2$/FTO (iii) for Ag-TiO$_2$/TiO$_2$ sol-gel /FTO (iv) for Ag-TiO$_2$/TiO$_2$ NPs/FTO. (c) EIS spectra of Ag-TiO$_2$/TiO$_2$ NPs at different frequencies under light (L) and dark (D), (d) Mott−Schottky (M-S) plot of Ag-TiO$_2$/TiO$_2$ NPs at different frequencies under dark condition.*

The stability of the Ag-TiO$_2$ sample with TiO$_2$ NPs thin film was carried out in 1 M KOH for 100 minutes under continues light illumination, which shows the photocurrent initially decreases and then it saturates. This study indicates the long-time stability of these Ag-TiO$_2$ thin films **(Figure 3.7(a)).** TiO$_2$ is very stable under catalytic reaction and the Ag nanoparticle is surrounded by TiO$_2$ matrix and enhances the overall catalytic stability of the Ag NP. However, there are some chances of partial oxidation of Ag nanoparticle at long time operation. Time response of different photoanode under light (100 mW/cm^2) and dark with -0.3 V external bias has been shown in **figure 3.7(b),** which indicates that the photoresponse is repeatable. Rise and fall time of Ag-TiO$_2$/TiO$_2$ NP/FTO sample is 0.6 S and 1.6 S respectively that implies that fast response of these devices. Summary of rising time and fall time of all samples are shown in **table-3.5**.

3.3   Conclusions.

In summary, efficient Plasmon-induced hot-electron generation and transfer have been observed in a solution-processed *in situ* grown Ag–TiO$_2$ thin film that has been utilized for enhanced solar H$_2$ generation. This growth technique requires three successive steps that include the fabrication of Li$_4$Ti$_5$O$_{12}$ ceramic thin film by sol-gel technique followed by an ion-exchange process that replaces Li$^+$ by Ag$^+$ to form Ag$_4$Ti$_5$O$_{12}$ thin film. Finally, Ag$_4$Ti$_5$O$_{12}$ thin-film converted to Ag -TiO$_2$ due to the reduction process of Ag$^+$ to Ag^o. Such kind of *in situ* growth of Ag NPs inside the TiO$_2$ matrix allows larger interface area formation between Ag NPs and TiO$_2$ with lesser interface trap state. The formation of Ag-TiO$_2$ was confirmed by SEM, XRD, XPS and UV-VIS absorption study. Photoelectrochemical measurements were carried of this Ag-TiO$_2$ thin film photoanodes to identify its applicability for H$_2$ generation. Our optimized Ag-TiO$_2$photoanodes showed a high photocurrent of density 42 mA cm^{-2} in 1M KOH solution under 0.45 V external bias which more than three orders higher than pure TiO$_2$photoanode. This current density is significantly higher than the recently reported Ag/TiO$_2$ system. The IPCE spectrum in visible range shows a strong photocurrent generation in the region of plasmonic absorption of Ag NPs, reveal that the major contribution to solar hydrogen generation is coming from the plasmon-induced hot-electron. Moreover, this photocurrent shows good stability that has been tested for more than 1.5 hours. In futuristic, the present process can be extended for the fabrication of other metal-metal oxide and metal chalcogenides-metal oxide composite systems for energy-related applications.